ELSEVIER

Journal of Nuclear Materials 282 (2000) 97–111

journal of nuclear materials

www.elsevier.nl/locate/jnucmat

Multiple voltage electron probe microanalysis of fission gas bubbles in irradiated nuclear fuel

M. Verwerft *

Reactor Materials Research Department, SCK.CEN, Boeretang 200, B-2400 Mol, Belgium

Received 10 January 2000; accepted 25 September 2000

Abstract

The accurate analysis of locally retained fission gas in nuclear fuel is inherently difficult since the physical form under which it is stored varies from an atomic dispersion to bubbles with a diameter of several hundreds of nanometers. One of the techniques that has been applied since more than 20 yr is electron probe microanalysis (EPMA). This technique, however, is difficult to apply in a quantitative manner if the studied materials are inhomogeneous at the scale of the electron–solid interaction volume. In this paper, a method is developed to analyse a system of gas bubbles distributed in a solid matrix. It is based on the geometric modelling of a gas bubble dispersion and the assessment of its influence on the emitted X-ray intensity. The calculation exploits experimental results acquired at different accelerating voltages. The resulting more accurate analysis of gas retained in nuclear fuel may lead to a better insight in the gas release mechanisms. © 2000 Elsevier Science B.V. All rights reserved.

PACS: 07.85.Nc; 07.78.+s; 82.80.Ej; 64.75.+g

1. Introduction

The behaviour of noble fission gases xenon and krypton and the role they play in the evolution of ceramic fuels with increasing burn-up has been the subject of numerous studies over the past decades. The noble gas atoms have a high fission yield and tend to escape from the matrix as they are insoluble in either UO_2 or $(U,Pu)O_2$. At low operating temperatures, their mobility is limited and they remain atomically dispersed. With increasing temperature, the gas atoms form bubbles of increasing diameter both at intragranular and intergranular sites, and a fraction escapes to the free volume of the rod. The formation of fission gas bubbles causes a swelling of the fuel pellets, which may result in pellet-cladding mechanical interaction. The gas escapes to the free pellets, which may result in pellet-cladding mechanical interaction. If the gas escapes to the free volume of the rod, then the internal pressure of the rod increases. In both cases the fuel rod integrity may be at risk. Debate still continues on the mechanisms that govern the redistribution of the noble gases and on how to predict their behaviour quantitatively. Given the large number of processes that play a role in the escape of fission gas, it is not surprising to find that a definitive model is not yet developed.

Important information on the fission gas behaviour is obtained from retained gas concentration profiles of individual pellets. Several analysis methods have been applied to study the fission gas behaviour (for a review, see e.g. [1]). The most common techniques are: electron probe microanalysis (EPMA) and X-ray fluorescence (XRF) on polished cross-sections of fuel pellets; scanning transmission electron microscopy and energy dispersive X-ray spectroscopy (STEM-EDS) on small samples taken at different positions from the pellet. To a lesser extent, also micro-coring and subsequent chemical dissolution or thermal treatment has been used. The spatial resolution differs widely between the different methods (micro-coring: $\simeq 500$ μm, XRF: $\simeq 30$ μm, EPMA: $\simeq 1$ μm and STEM: $\simeq 0.001$ μm), and the information that can be obtained by each method varies accordingly. For example, if entire cross-section analyses with subgrain resolution are needed, then only

---

* Tel.: +32-14 333 048; fax: +32-14 321 216.
E-mail address: mverwerf@sckcen.be (M. Verwerft).

PII: S0022-3115(00)00421-9

EPMA can provide the necessary information. The different analysis methods also provide information of a different kind: micro-coring and XRF yield bulk concentrations, while EPMA is a surface near analysis technique and by STEM thin foils are analysed. When comparing results from different methods [2], one may derive important information e.g. on the role of grain boundaries, but it is of major importance to know as accurately as possible what exactly is measured by each method. In this paper, we will focus on the problem of electron probe microanalysis of gas bubbles in a solid. The interpretation of the results, obtained with electron probe techniques, indeed needs to be performed with extreme care.

Two decades ago, Ronchi and Walker [3] showed that the clustering of fission gas and the formation of bubbles result in a loss of signal in EPMA analyses. In the same paper, they also derived a correction procedure using the Philibert expression for depth distribution of X-ray production and this correction procedure was applied in subsequent research campaigns [1,4]. The quantitative determination of bubble size distributions however is a time consuming task, and since the influence of the correction in many cases is limited, the correction procedure often can be considered to be unnecessary [2,5]. But even though the choice of appropriate analysis conditions limits the signal loss, the problem basically persists.

In the present paper, multiple voltage analyses are proposed as a simple method to judge the necessity to apply corrections to the measured Xe signal. One may then decide whether or not the specific problem calls for a more elaborate analysis and, if necessary, to apply a correction for the loss of signal due to the clustering of gas into bubbles. The correction procedure that is developed below, is based on a geometrical description of the bubble dispersion and uses the multiple voltage analyses. The geometrical description allows one to treat the problem using so-called 'phi-rho-Z' methods for X-ray depth distributions [6].

2. Electron probe microanalysis of Xe

2.1. Multiple voltage analyses

The Xe profiles were acquired with a CAMEBAX-R Microbeam instrument adapted for the analysis of radioactive samples, and controlled by the XMAS software of SAMx. Its spectrometers are internally shielded to reduce the background coming from the high gamma activity of irradiated fuel. Analyses are performed with high probe currents (typically 50–100 nA), and the PHA is operated in differential mode. As such, it is possible to obtain acceptable detection limits with reasonable counting times even on highly active samples. Quantitative wavelength dispersive spectroscopy (WDS) is based on comparison with standards. Since Xe standards suitable for EPMA analysis do not exist, the fluorescence yield is determined by interpolation, as described e.g., by Walker [7].

When analysing the Xe concentration on cross-sections of fuel rods that have been subjected to high linear power, one observes a pronounced drop of the Xe signal at the centre of the fuel pellet (Fig. 1). The thermal release of volatile fission products is a well-known phenomenon, and if one measures the composition of the gas in the free volume of the fuel rod, Xe is indeed found. On the basis of Xe-profiles, such as represented in Fig. 1, one may calculate the amount of released gas and compare the result with a direct analysis of the gas contained in the free volume of the fuel rod. The fission gas release, calculated on the basis of the profile of Fig. 1 and taking into account the axial form factor of the power during the transient test, is estimated as 29%. A direct analysis of the gas contained in the free volume shows a release of only 7%. The systematic underestimation of the xenon concentration by EPMA analyses is a known phenomenon and is attributed to both signal loss related to the formation of bubbles [3] and to the loss of grain boundary stored gas during sample preparation [4].

In a standard EPMA measurement, one chooses the accelerating voltage in order to minimize correction factors, and in general on overvoltage ratio between 2 and 3 is recommended [8]. In nuclear fuel, one is usually concerned with characteristic lines of energies between 2 and 6 keV, in which case an accelerating voltage of 10–15 kV would in theory be ideal. If the same analysis would be performed at different accelerating voltages, then one expects to obtain identical results, with a slight decrease of accuracy if the X-ray correction factors are

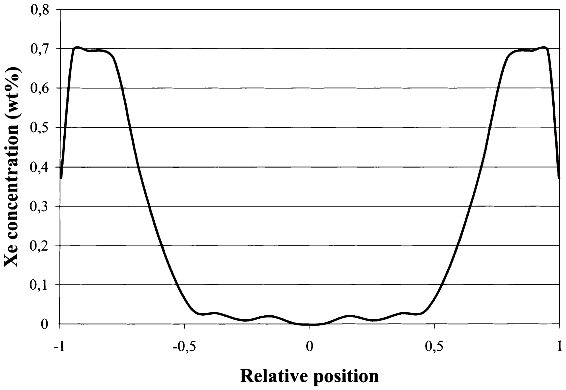

Fig. 1. Xe concentration variation as a function of radial position (top). The electron beam accelerating voltage was chosen as 15 kV. The scan is acquired on a cross-section of a fuel pin (bottom).

large. In some cases, however, the measured Xe concentration itself is function of the accelerating voltage. In Fig. 2, Xe profiles are shown for three high burnup fuel samples (approximately 55 GWd/tM), each with a different irradiation history and microstructure. It is not surprising to find that the profiles of retained Xe are different for each sample, but it is quite unexpected to find that the experimental conditions of the analysis have a major influence on the profile in one case (Fig. 2(c)), while they have only a moderate influence (Fig. 2(b)) or no influence at all (Fig. 2(a)) in other cases. The essential parameters of the fuel and its irradiation characteristics are summarised in Table 1.

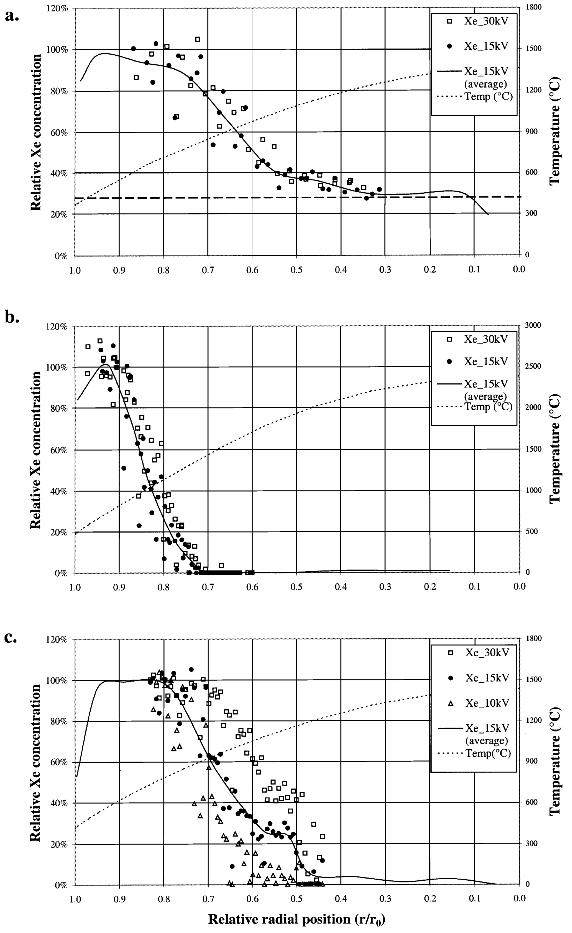

Fig. 2. Variation in apparent Xe concentration as a function of radial position for different accelerating voltages. The three figures display the profiles for three different fuel pins, each with a different irradiation history and/or microstructure. Details about the fuel and irradiation history are given in Table 1. The solid line shows the radially averaged 15 kV Xe profile. The dotted line displays the calculated radial temperature profile. (a) Xe profiles of sample A. The analysis conditions do not influence the measured retained Xe profile. The dashed line represents the concentration of Xe generated during the last quarter of its burnup accumulation. (b) Xe profile of sample B. The Xe profile show a slight dependence on accelerating voltage in the transition zone. (c) Xe profile of sample C. In the transition zone, the Xe profile is largely influenced by the applied accelerating voltage due to substantial intragranular bubble development.

The sample of Fig. 2(a) was taken from a fuel rod that had experienced a relatively high linear power (35 kW/m) during 113 h at a burnup of 40 GWd/tM, i.e., at about three quarter of its end-of-life burnup. During this period, its centerline temperature raised to 1375°C and an important fraction of its fission gas (21%) was released. The last quarter of the irradiation was performed at a lower linear power level and no additional gas was released. The retained fission gas profile of Fig. 2(a) reflects this power history. At the periphery, the measured amount of Xe equals the generated quantity. In the region $0.75 \geqslant r/r_0 \geqslant 0.4$, the retained fraction gradually decreases to a constant value slightly less than 30%, which equals the amount generated after the power transient. Post-irradiation examination of the fuel by scanning electron microscopic (SEM) observations failed to reveal intragranular bubbles all along the pellet radius, and the EPMA profiles of retained Xe do not depend on the applied accelerating voltage.

The rod from which the sample of Fig. 2(b) was taken, experienced a power transient of 60 kW/m during 24 h and its end-of-life. The fission gas is retained only in the outer regions and shows a sharp drop to zero retention between $0.9 \geqslant r/r_0 \geqslant 0.7$. In this transition zone, microscopic observations showed intragranular bubbles in the region $0.85 > r/r_0 > 0.75$. At the position where intragranular bubbles were found, the EPMA profiles acquired at different accelerating voltage also show a slight difference.

The sample of Fig. 2(c) is taken from a fuel rod with large grained fuel (40 μm) which was base irradiated up to 56 GWd/tM at relatively low power and experienced a power transient of 35 kW/m during 24 h at its end-of-life. After the base irradiation, the fission gas release was found to be 1.9% in a sibling rod with the same microstructure and irradiation history. After the transient test, the fission gas release was 7%. The retained gas profile shows that at radial positions $r/r_0 \geqslant 0.8$, the measured Xe concentration equals the generated amount and the measured amount of Xe is independent of the applied analysis conditions. At positions $r/r_0 \leqslant 0.5$, the Xe concentration approaches zero, again irrespective of the experimental conditions. In the transition zone, however, the apparent Xe concentration depends on the applied accelerating voltage: the higher the applied potential, the higher the measured Xe concentration. The difference between an analysis performed at 30 kV and one performed at 10 kV is maximal at relative radius $r/r_0 = 0.65$ and amounts to more than 50%. The microscopic examinations of this sample showed

Table 1
Fuel pellet and rod characteristics

	A	B	C
Rod type	BWR	BWR	BWR
Pellet diameter (mm)	10.36	10.36	10.52
Enrichment (%^{235}U)	4.9	4.9	3.2
Pellet density (% TD)	95.5	95.5	95.5
Grain size (μm)	10	10	40[a]
Diametrical gap (μm)	192	192	132
Cladding	Zry-2 + Zr liner	Zry-2 + Zr-liner	Zry-2
Fill gas (He) pressure (MPa)	2	2	0.3
Burn-up (GWd/tM)	55	55	56
Base irradiation conditions (kW/m)	$\simeq$ 30	$\simeq$ 30	<30
Max LHGR (kW/m)	35	60	35
Burnup at max LHGR (GWd/tM)	40	EOL	EOL
Hold time of max LHGR (h)	113	24	24

[a] Large grain sizes were obtained by doping with Nb_2O_5 and applying an elevated relative moisture (85% at 25°C) in the sintering atmosphere.

extensive intragranular bubble development in the region $0.85 > r/r_0 > 0.45$, i.e., in the region where the measured Xe signal is a function of the accelerating voltage.

In this paper, it will be shown that it is indeed the development of intragranular bubbles that results in a spurious loss of Xe signal and it will also be shown how radial Xe profiles acquired at different accelerating voltages may be exploited not only to detect this effect, but also to account for it quantitatively. We will essentially work with the experimental results obtained from sample C, which has a grain size that is considerably larger than usual, offering the possibility to separate grain bulk effects from grain boundary influences. Throughout the study, all EPMA data were acquired exclusively from the centre of individual grains taking care that the grain boundaries are not hit by the electron beam.

Qualitatively, one may understand the effect caused by the accelerating voltage by looking at the difference between SEM images acquired at different applied voltages. At low accelerating voltages (Fig. 3(a)), only those bubbles are visible that intersect the free surface, at higher voltages on the other hand (Fig. 3(b)), one also observes sub-surface bubbles. Since the bubbles that intersect the free surface obviously do not contain any Xe, there is a concentration gradient between the very surface where the Xe content is zero and depths larger than the bubble diameter, where the gas in the bubbles is preserved (Fig. 4). Since at higher accelerating voltages the electrons penetrate deeper into the material, it is clear that increasing the accelerating voltage results in a higher apparent Xe concentration.

In order to appreciate the approach that is worked out in the following paragraphs, the depth distribution of both excited and emitted X-rays at different accelerating voltages will first be assessed. In Figs. 5(a)–(d) the generated and emitted distributions are given for the $Xe_{L\alpha}$ signal at different accelerating voltages ranging

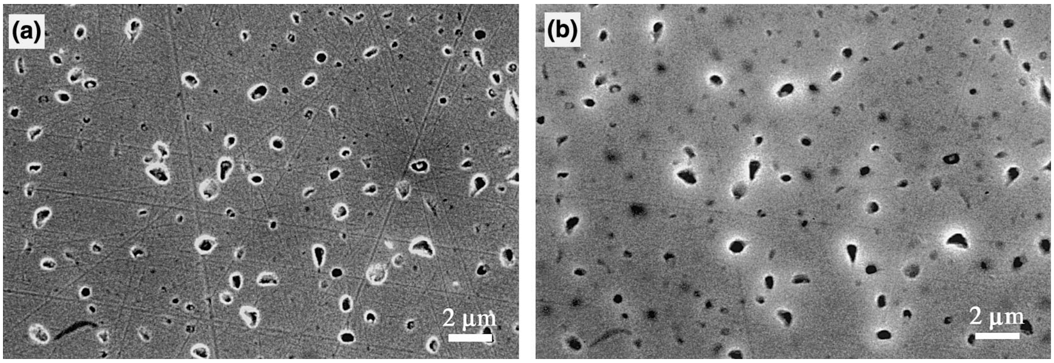

Fig. 3. Influence of the accelerating voltage on the details revealed on a polished cross-section. Both images are made exactly at the same position, but with different primary beam accelerating voltage. (a) H.T. = 7 kV, the image only reveals the bubbles that intersect with the surface. (b) H.T. = 30 kV, in addition to the bubbles that intersect the surface, also subsurface Xe-filled bubbles are visible as dark spots.

from 10 to 50 kV. All calculations are performed for a homogeneous distribution of Xe in a UO_2 matrix with a density of 10.96 g/cm^3. If a low accelerating voltage of 10 kV is applied, then the emitted X-ray distribution almost equals the generated distribution and the maximal depth is about 0.3 μm (Fig. 5(a)). With increasing primary beam voltage, X-rays are also generated at larger depths: up to 0.7 μm at 15 kV, 1.1 μm at 20 kV, 2.4 μm at 30 kV and 5.5 μm at 50 kV. It is also clear that at high accelerating voltages the emitted signal is only a small fraction of the generated X-rays. One also perceives that while the maximal probed depth increases by a factor of 18 when increasing the accelerating voltage from 10 to 50 kV, an important fraction of the emitted X-ray signal is generated in the top layer even for high accelerating voltages. Hence, it is more useful to consider the cumulative depth distribution curves of the emitted signal rather than the maximal depth of X-ray generation (Fig. 6). From these curves one can read the fractional contribution to the emitted X-rays of a top layer of given thickness. The thickness of the layer which accounts for 90% of the total emitted signal is 0.16 μm at 10 kV, 0.32 μm at 15 kV, 0.45 μm at 20 kV, 0.76 μm at 30 kV and 1.10 μm at 50 kV. The contribution to the total signal which is generated in the first 100 nm amounts to 72% at 10 kV, it drops to 44% at 15 kV, but still accounts for 20% at 30 kV and 15% at 50 kV.

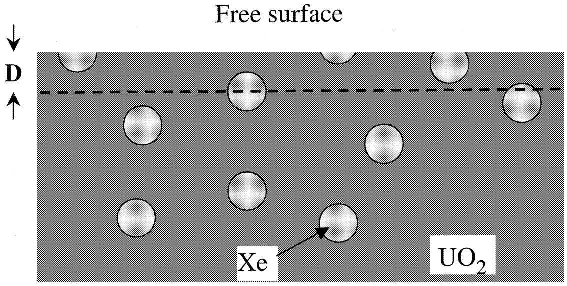

Fig. 4. Schematic representation of the influence of bubble formation on the residual Xe concentration close to the free surface of a sample. At the very surface, only open bubbles are found and at depths larger than the bubble diameter ⟨D⟩, all bubbles are closed.

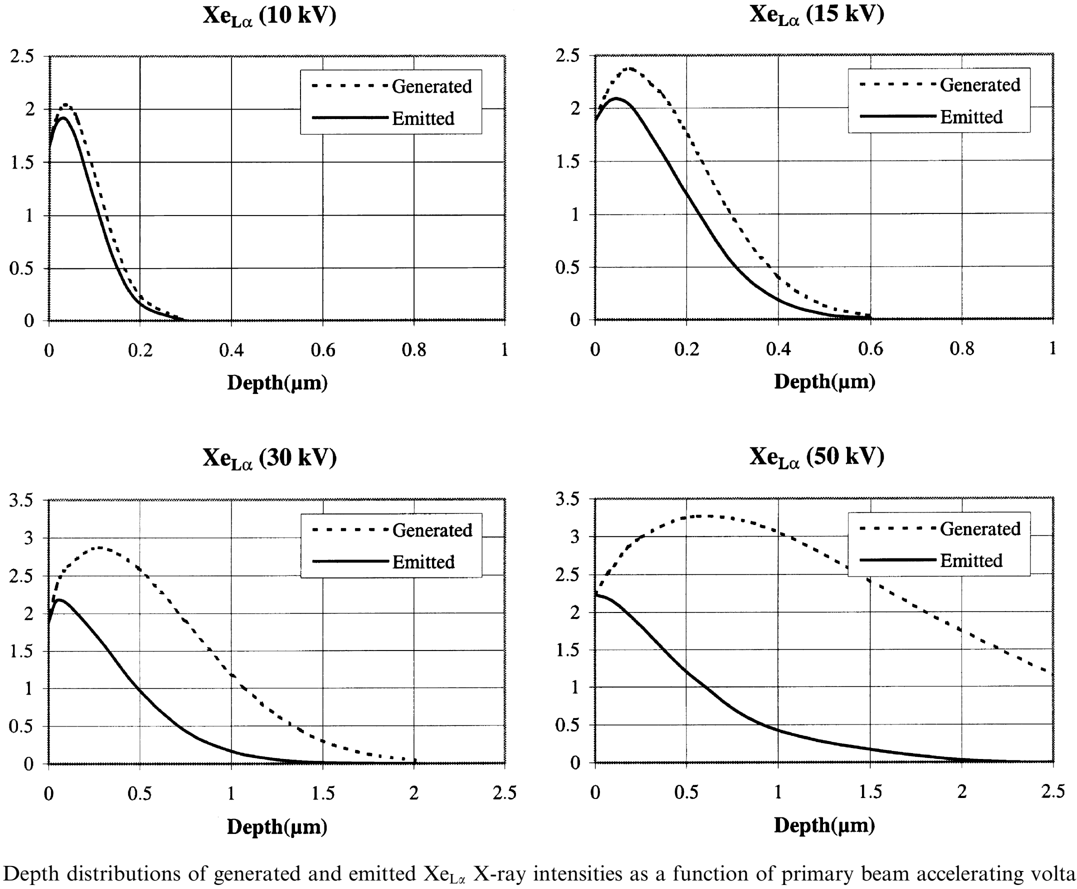

Fig. 5. Depth distributions of generated and emitted $Xe_{L\alpha}$ X-ray intensities as a function of primary beam accelerating voltage. The calculations are performed in the assumption of atomic dispersion of the solute atoms (Xe) in the matrix (UO_2).

As is schematically represented in Fig. 4, the precipitation of noble gas in bubbles will give rise to concentration gradients near the surface of the sample and hence influence the EPMA analysis. Since the bubbles have characteristic diameters ranging from a few nm to several hundreds of μm, it is clear from the above discussion on the probing depth by EPMA that the measured signal will be affected by the bubble formation, whatever the experimental conditions be. In the paper, it will be shown that if one exploits the fact that different depths are probed when different accelerating voltages are used, one may extrapolate the measured signal to the true bulk value of Xe retained in bubbles.

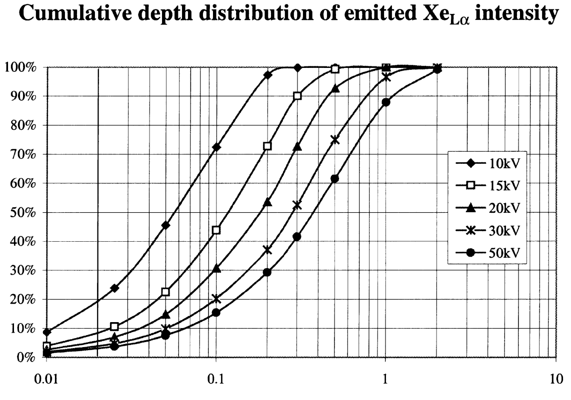

Fig. 6. Cumulative depth distribution of emitted Xe$_{L\alpha}$ X-ray intensity for different primary beam accelerating voltages.

2.2. Modelling the bubble distribution

SEM observations of sample C (Fig. 7) show that the bubble size distribution varies with the radial position. At radial position $r/r_0 = 0.69$ (Fig. 7(a)), intragranular bubbles with an average diameter of 200 nm are homogeneously dispersed. Some larger, well-separated lenticular bubbles decorate the grain boundaries. At radial position $r/r_0 = 0.65$ (Fig. 7(b)), bubbles have coarsened to an average diameter of 300 nm, but are still

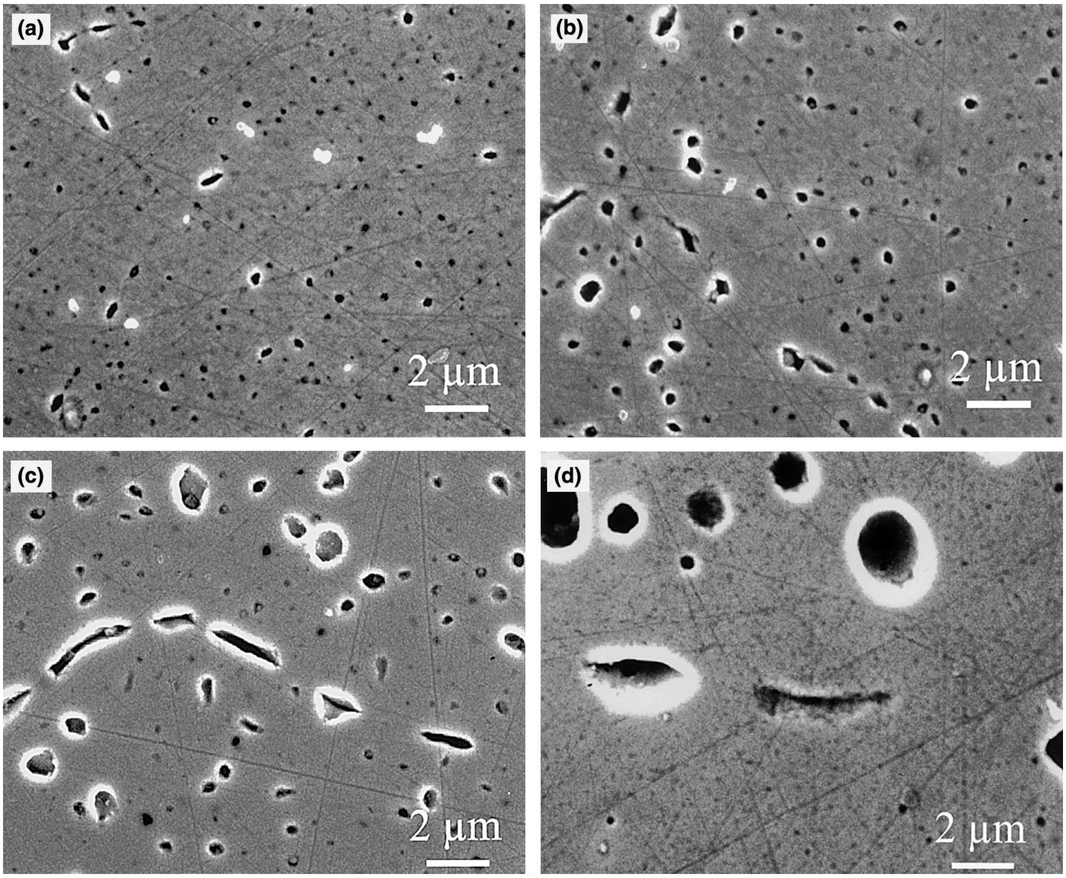

Fig. 7. SEM images showing the variation in bubble size distribution with radial position (sample C): (a) radial position $r/r_0 = 0.69$; (b) $r/r_0 = 0.65$; (c) $r/r_0 = 0.55$; (d) $r/r_0 = 0.09$.

distributed homogeneously, and grain boundary decoration is more pronounced. At $r/r_0 = 0.55$ (Fig. 7(c)), the average bubble diameter is 500 nm, and grain boundary bubbles are more abundant and at least partially interconnected. Fig. 7(d) shows the morphology at the pellet centre ($r/r_0 = 0.09$). Large bubbles have developed inside grains (their average diameter is 1.5 μm), and large interconnected pores decorate the grain boundaries.

At each radial position, a distribution of bubble sizes is found. The structure we are thus dealing with, is a polydispersed system of spheres filled with a (probably highly pressurised) noble gas mixture in a ceramic matrix (Fig. 8(a)). Apart from the gas spheres, numerous other precipitates are present in the UO_2 matrix, and a number of elements remains atomically dissolved. We will, however, neglect the minor influence of the other fission products on the Xe signal and consider only the gas filled spheres and the UO_2 matrix.

In the early days of electron microprobe analysis, quantitative analysis was performed with the aid of the so-called ZAF correction methods that essentially use the depth distribution profile for generated X-rays described by Philibert [9]. These methods provide satisfying results for samples which are homogeneous on the scale of the electron–solid interaction volume and for which the absorption of generated X-rays is weak. For samples which are inhomogeneous in depth or in which absorption is high, the ZAF corrections are not appropriate since the profiles calculated on basis of the Philibert model are too crude a representation of the true depth distribution of the primary X-ray generation. The X-ray model developed in [3] to account for the clustering of Xe in nuclear fuel made use of this Philibert expression and as a consequence of the limitations of this expression, the variation of the emitted Xe signal with accelerating voltage was not correctly predicted. During the 80s, several researchers [10–15] developed X-ray models that improve on the Philibert approach. With the development of the so-called ‘phi-rho-Z’ X-ray correction models, electron microprobe analysis of layered structures (2D homogeneous systems) became possible. However, a straightforward correction model to analyse systems that are truly inhomogeneous in three dimensions does not exist. In the case of retained fission gas analysis, one is interested to know the average concentration of Xe in a zone with a specific bubble distribution. Experimental electron probe analyses of such systems are therefore usually performed with either a defocussed beam or a scanning probe which covers an area of several tens to a few hundred μm^2, to obtain an average Xe concentration of a substantial volume. Although it is well-known that this method does not provide a true average, since the X-ray correction factors vary with the local composition, this wide beam averaging is common practice. We will now develop a mathematical description of such a 3D inhomogeneous system in order to be able to apply X-ray correction models.

Let us consider the generated primary X-ray intensity along a line A_i perpendicular to the sample surface (Fig. 8(a)). A line crossing a polydispersed system of

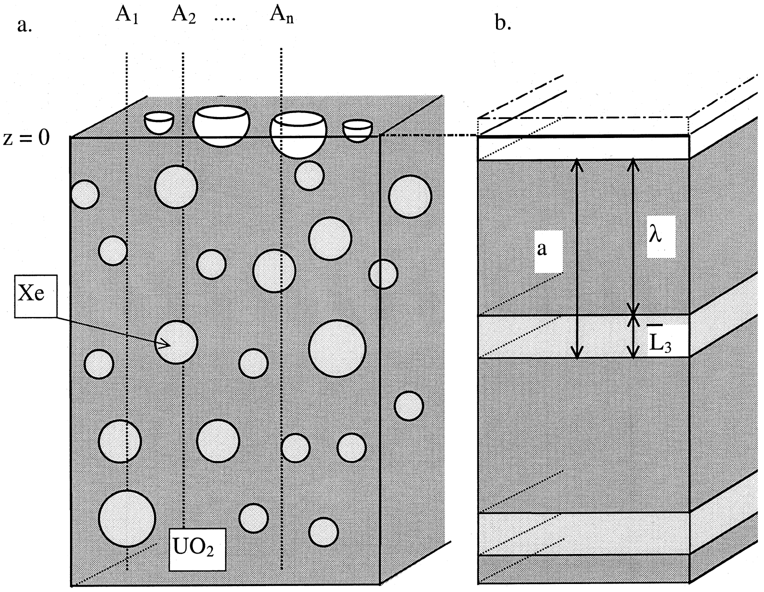

Fig. 8. (a) Schematic representation of the bubble configuration: the ceramic matrix is dark grey, closed bubbles are light grey and open bubbles are white. Vertical intersections (A_i) are also drawn. (b) Averaged linear intersection, with a schematic representation of the linear parameters $\overline{L_3}$ and λ, and the period a.

spheres will intercept the particles with a mean intercept length (see e.g. [16])

$$\overline{L_3} = \frac{2}{3}\langle D \rangle \tag{1}$$

with $\langle D \rangle$ the average diameter of the spheres. The mean free edge- to-edge distance between two intercepts reads as

$$\lambda = \frac{2}{3}\langle D \rangle \left(\frac{1 - V_V}{V_V} \right) \tag{2}$$

with V_V the volume fraction of spheres.

An average linear section (Fig. 8(b)) through the matrix can thus be described as a periodic sequence with period

$$a = \overline{L_3} + \lambda \tag{3}$$

and the density function for the unit cell reads as

$$\begin{aligned} \Re(\xi) &= \rho_{UO_2} \quad \text{for} \quad 0 < \xi \leqslant \lambda, \\ &= \rho_{Xe} \quad \text{for} \quad \lambda < \xi \leqslant a, \\ &= 0 \quad \text{elsewhere.} \end{aligned} \tag{4}$$

For the density of the matrix, the theoretical value should be taken ($\rho_{UO_2} = 10.96\ \text{g/cm}^3$), and the density of the gas inside the bubbles has to be determined from iterative calculations.

The one-dimensional structure (Fig. 9, left) can thus be written as

$$\rho_0(z) = \sum_n \Re(z - n \cdot a), \quad \text{with} \quad n = \text{integer}. \tag{5}$$

The structure defined in (5) is infinite in all dimensions: it is homogeneous alone x and y and varies periodically along z.

2.3. Implementing an X-ray correction procedure for a bubble distribution

A microprobe analysis is performed on a polished sample and the penetration depth of the electron beam is of the same order of magnitude as the parameters $\overline{L_3}$ and λ. It is therefore crucial to take into account the effect of the intersection of the structure described by Eq. (5) with the free surface of the sample. This interaction will indeed largely influence the measured X-ray intensity. To account for the effect of the free surface, one must calculate the X-ray intensity for all possible intersection configurations (Fig. 9). In practice the number of different configurations that have to be calculated (N_c) is determined by convergence criteria. The density function of the ith configuration reads as

$$\rho_i(z) = \rho_0(z - \Delta_i) \quad \text{with} \ \Delta_i = \frac{ia}{N_c}, \tag{6}$$

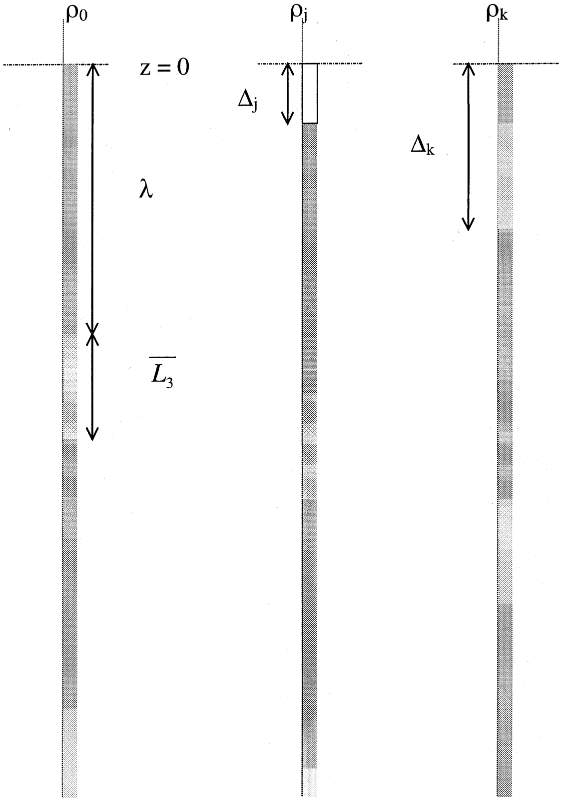

Fig. 9. Different configurations of the same 1D representation of a bubble distribution. Each configuration is defined by the position of the zero level ($z = 0$). Symbols in the figure refer to formula (6).

N_c being the number of configurations $i = 0, 1, \ldots, N_c - 1$.

A bubble which intersects with the free surface no longer contains Xe (Fig. 9, middle). The sample preparation also involves grinding and polishing, which damages the top layer and Xe will thus also be lost from bubbles which are entirely closed, but which intersects with this damaged zone. If the bubbles are in overpressure, then they can only remain intact if the covering layer is strong enough to counteract the internal pressure. To account for these effects, a depleted layer with thickness δ is assumed.

Since the hypothetic 1D structure is built on the average intersection which occurs off-center, the topmost position of a closed Xe-'layer' is found at depth (see Fig. 10)

$$h = \frac{1}{6}\langle D \rangle + \delta = \frac{1}{4}\overline{L_3} + \delta. \tag{7}$$

This condition may be introduced in (6) by imposing that

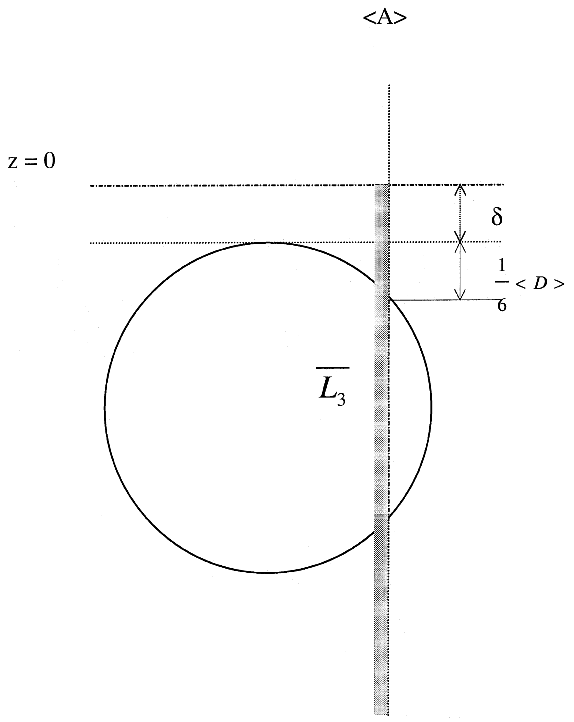

Fig. 10. Schematic drawing showing the topmost position of an intact bubble and how this configuration is represented in the corresponding 1D representation.

$$\rho_{\mathrm{Xe}}(z) = 0 \text{ for } z \leqslant \Delta_i \text{ and } \Delta_i \leqslant \overline{L_3} + h = \frac{5}{4}\overline{L_3} + \delta. \tag{8}$$

For each configuration (6) and taking into account the condition (8), the X-ray intensities of uranium, oxygen and xenon are then calculated and averaged

$$I_\alpha = \frac{1}{N_c}\sum_{i=0}^{N_c} f_\alpha(\rho_i(z)) \quad \alpha = \mathrm{U, O, Xe}. \tag{9}$$

In this expression, $f_\alpha(\rho_i(z))$ is the calculated k-ratio for the considered element (α) for a configuration (i). These calculated X-ray intensities (expressed as k-ratios) are finally used as input to determine the apparent Xe concentration for a given bubble distribution. For the present study, we have implemented (9) using the parabolic PAP method, according to the approach described in detail in [6]. Mass absorption coefficients are taken from [17].

In Fig. 11, the results are represented of model calculations showing the variation of the apparent gas concentration as a function of bubble diameter. It should be noted that the bulk Xe concentration is kept constant. The fundamental aspects of the calculated curves of Fig. 11 are identical to those of the experimental curves of Fig. 2(c). When the gas is dispersed atomically, the measured Xe concentration is independent of the accelerating voltage. when bubbles develop, the Xe signal is reduced and becomes a function of the accelerating voltage: the lower the applied accelerating voltage, the lower the apparent Xe concentration.

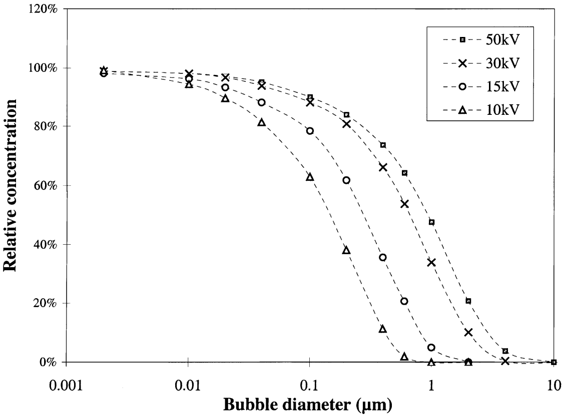

Fig. 11. Calculation of the X-ray intensity yield as a function of bubble diameter. The difference between 10 and 30 kV is maximal for bubbles of diameter 400 nm and amounts to more than 50%. The bulk Xe concentration is kept constant and the calculated reduction in signal is thus the sole result of bubble information and growth. The apparent Xe concentration continues to rise with accelerating voltages but it will never be possible to obtain the true bulk value due to the limited escape depth of the $\mathrm{Xe}_{\mathrm{L}\alpha}$ line.

2.4. Discussion of the model parameters and calculated X-ray intensities

The X-ray intensity calculation (9) makes use of several parameters defined in expressions (1)–(8). The independent parameters are:

- bubble diameter ($\langle D\rangle$);
- bubble volume fraction (V_V);
- number of configurations (N_c);
- density of the gas (ρ_{Xe});
- thickness of the depleted layer (δ).

They are discussed below.

- The bubble size distribution is described by two parameters $\langle D\rangle$ and V_V, which both vary with radial position. For the example presented in this paper, the bubble size distributions are determined on the basis of SEM observations of the polished fuel pellet cross-section. However, one should remember that small bubbles and nanoclusters remain unresolved in a SEM analysis. A second limitation is the fact that SEM observations provide only a two-dimensional analysis of the sample. The 3D distribution parameters must be derived by stereological calculations. We have used the Saltykov area analysis method (see e.g. [16]) to determine the true size distribution at different radial positions. From these size distributions,

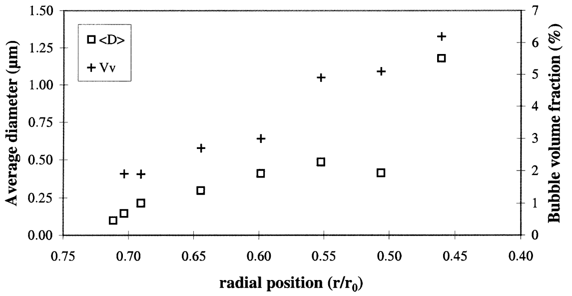

Fig. 12. Variation with radial position of the average bubble size and bubble volume fraction for sample C.

one may then derive the local average diameter $\langle D\rangle$. Its variation with radial position is represented in Fig. 12.

- The bubble volume fraction, V_V, can either be calculated from the derived bubble size distribution or directly measured. The volume fraction of a polydispersed system of spheres (V_V) is equal to the area fraction (A_A) of the intersection of these spheres with the plane of polish. The area fraction, A_A, equals the sum of the areas of all circular sections divided by the total area analysed. The variation with radial position of the bubble volume fraction is also represented in Fig. 12.
- The number of configurations (N_c) is imposed by convergence criteria. If one uses as criterion that the convergence should be within 1%, then N_c should be chosen such that

$$\frac{\overline{L_3}+\lambda}{N_c} < 20\ \text{nm}. \tag{10}$$

- For a known concentration of gas and bubble volume fraction, the gas density is fixed by dividing the weight percentage by the bubble volume fraction. The bulk concentration of Xe obviously is not known beforehand, and has to be calculated iteratively. In a first approach, the generated X-ray intensity is calculated assuming complete retention of the produced fission gas. The calculated X-ray intensity is then compared to the experimental value, and the calculation is iterated. It was found that the gas density only marginally affects the correction factors related to the bubble distribution, hence this iteration converges rapidly.
- The thickness δ of the depleted layer is difficult to calculate independently as it is a function of both bubble pressure and sample preparation. In the case of overpressurised bubbles, gas may be released due to the mechanical instability of a pressurised bubble close to a free surface. The stress in a thin layer of width w between the free surface and a bubble of radius R and internal pressure p is given by

$$\sigma = \frac{(p-(2\gamma/R))R}{2w}. \tag{11}$$

In this expression, γ is the solid–gas surface tension.

A bubble will remain closed as long as the stress σ is smaller than the critical fracture stress σ_c of UO_2. The condition on the width w reads thus as

$$w \geqslant w_1 = \frac{p\cdot R-2\gamma}{2\sigma_c} \tag{12}$$

It is clear that for bubbles in thermodynamic equilibrium, w_1 will vanish. Experimental results reported by Thomas [18] and Kashibe et al. [19], show that equilibrium is reached only in large bubbles. They also show that pressure rapidly rises for smaller bubbles, in which case one may neglect the term 2γ in expression (12) and w_1 becomes proportional to the product of the bubble pressure and radius. The proportionality factor $1/2\sigma_c$ however is poorly known. The theoretical value for the critical fracture stress σ_c in UO_2 equals 3.0×10^{10} N/m^2, while experiments show that fracture occurs at stresses of about 1.4×10^{8} N/m^2, i.e., 200 times smaller. The large discrepancy is explained by assuming that small flaws are present at the surface of the test specimens [20]. While the theoretical value may be appropriate for nm-size bubbles, the much lower macroscopic value should be used when stability of larger bubbles is considered. Since there exists no criterion that defines the range of application of either of the two values, it is not possible to calculate w_1 reliably.

The problem is even more complicated, since not only overpressurised bubbles are unstable close to the free surface, but the sample preparation itself introduces damage. Again, the degree to which grinding and polishing introduces damage to sub-surface bubbles will depend on the local bubble size. No effect is expected in the case of atomically dispersed Xe, while large bubbles may be more easily damaged by the sample preparation process. This can be expressed by an effective damaged zone with w_2

$$\begin{aligned} &w_2 = 0 \quad \text{for atomically dispersed gas,}\\ &w_2 = f(\langle D\rangle) \quad \text{where bubbles have developed.} \end{aligned} \tag{13}$$

Combining the sample preparation induced damage with the bubble stability condition results in a depleted layer width $\delta = w_1 + w_2$. In view of the fact that neither of the parameters w_1 and w_2 can be calculated with confidence, an experimental method to estimate its value was searched for. It is possible to estimate the value of δ when taking full advantage of the multiple voltage analyses.

If one takes the ratio of analyses performed at different accelerating voltages, the influence of the geometry is separated from concentration variations. The ratios of the apparent Xe concentrations (10 kV/30 kV

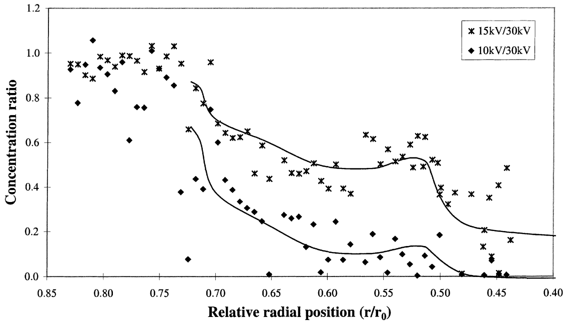

Fig. 13. Ratio of the concentration profiles as a function of relative radial position. The markers represent experimental data, and the curves are calculated on the basis of the bubble size distribution data of Fig. 12 and with a depleted layer width δ as expressed in formula (14a) and (14b).

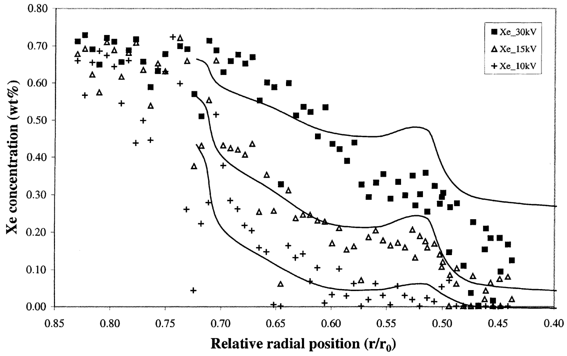

Fig. 14. Calculated (solid lines) and experimental (markers) variation in apparent Xe concentration as a function of radial position and accelerating voltage. The calculated values are obtained on the basis of bubble size evolution observations (Fig. 12), assuming complete bulk retention of Xe.

and 15 kV/30 kV) are represented in Fig. 13. At radial positions $r/r_0 > 0.80$, the ratios 15 kV/30 kV and 10 kV/30 kV are equal to 1, which is to be expected in the case of atomically dispersed Xe. When bubbles develop, both ratios decrease and the decrease is larger and starts earlier for the 10 kV/30 kV ratio than the 15 kV/30 kV ratio. At mid radial position ($r/r_0 = 0.50$), the 15 kV/30 kV ratio shows a remarkable rise. If one compares Fig. 13 with the graph showing the bubble size evolution (Fig. 12), then it appears that at the same position, the average bubble size is smaller than at the two adjacent points of observation. The good correspondence between features observed in Figs. 12 and 13 confirms that concentration ratio profiles indeed are sensitive to the local geometry of the Xe distribution.

In Fig. 13, the calculated concentration ratios are also given (solid lines). A good correspondence between experimental and calculated ratios was obtained for

$$\delta = 0.2\langle D\rangle \quad \text{for} \quad r/r_0 > 0.65, \tag{14a}$$

$$\delta = 80\ \text{nm} \quad \text{for} \quad r/r_0 < 0.65. \tag{14b}$$

This is qualitatively in accordance with the expected behaviour discussed above: for smaller bubbles (14a), the pressure related stability condition (12) essentially holds, while for larger bubbles (14b), damage due to polishing governs the Xe release from sub-surface bubbles (expressed in 13).

3. Discussion

At this point, all parameters needed for the model calculations are known. Let us first consider the reduction in apparent Xe concentration related to bubble formation and growth. In Fig. 14, calculated curves are compared with experimental data points. The computed curves are obtained under the assumption of complete retention. The calculated reduction in apparent Xe concentration is thus solely the result of the agglomeration of Xe in bubbles and is not related to a true release of fission gas. The general trend of the experimental data (Fig. 2(c)) agrees very well with the calculated curves (Fig. 14) for all three accelerating voltages. The loss of signal as observed experimentally is thus at least partly related to the formation of bubbles.

For radial positions $r/r_0 > 0.8$, the Xe concentration reaches a plateau, and the measured concentration is independent of the applied accelerating voltage. More towards the pellet centre ($r/r_0 < 0.8$), the apparent Xe concentration starts falling: first for the lowest accelerating voltages, then also for the higher ones. SEM observations in this zone reveal bubble formation only at positions $r/r_0 \leqslant 0.7$. Indirectly, we have thus evidence for the presence of very small bubbles, which remain unresolved in a SEM analysis. TEM observations have indeed shown that in the early stage of bubble formation during transient tests, nm-sized gas filled clusters are formed (see e.g. [18,19,21]). Such clusters are of course not revealed by a SEM analysis, but the X-ray signal seems to be sensitive even to the formation of very small clusters, especially when the analysis is performed at a low accelerating voltage. TEM investigations have also shown that in the early stage of bubble growth, only a fraction of the bubbles coarsen, while another fraction stays at the nm scale [21,22]. Some caution is thus in order when evaluating the lower tail of bubble size distributions determined by SEM. From radial position $r/r_0 < 0.6$ on, the calculations systematically overestimate the experimental results, which indicates true release of intragranular Xe. On going further towards the pellet centre, the Xe value continues to decrease even for high accelerating voltage analyses. SEM observations (Figs. 7(g) and (h)) show an increasing fraction of intergranular porosity, which is excluded from the

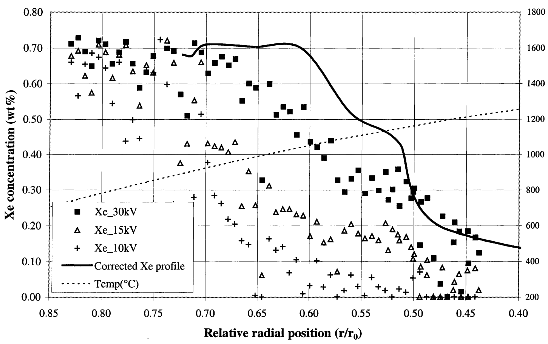

Fig. 15. Experimental (markers) and corrected (solid line) Xe concentration profile. One observes that retained gas fraction is systematically underestimated in the region between $r/r_0 = 0.7$ and $r/r_0 = 0.5$ at all three accelerating voltages used.

present analysis, and for which it is known that EPMA is not the appropriate tool to investigate the eventually retained gas fraction. Other methods such as e.g. X-ray fluorescence should then be applied [23]. In the present example, however, there is a broad transition zone in which the signal loss to a large extent is due to intragranular bubble formation and for which the calculation developed above applies.

Once the influence of the bubble formation on the Xe X-ray intensity is known, one may compensate for it. In Fig. 15, the corrected Xe profile is given, together with the raw data. It is clear that at low accelerating voltage, the as-measured profiles highly underestimate the amount of retained fission gas, but the difference between the raw profile and the one obtained after compensation for the signal loss decrease at higher accelerating voltages. On the basis of radial profiles such as those of Fig. 15 and taking into account the axial power variation during the transient-test one may calculate the total amount of released fission gas. On basis of the raw profile acquired at 15 kV, a release of 29% is expected. The 30 kV data lead to an estimated release of 16% and the corrected profile yields a release of 11%. Latter value is still higher than the amount of released gas as measured by puncturing the fuel rod, which yielded a release of 7%. As the present method only compensates the signal losses of the intragranular fraction of retained gas, it is not surprising to find that the EPMA based method still underestimates the truly retained gas fraction.

While the need for applying an elaborate correction of the EPMA data may not be obvious if only a gross Xe profile or a retained fission gas fraction is looked for, its necessity may be better appreciated in combination with observations of the grain boundary bubble evolution (Fig. 16). At radial position $r/r_0 = 0.65$ (Figs. 7(c) and (d) and 16(a)) grain boundary bubbles are well developed, but are not yet interconnected. If the EPMA data were used directly, i.e., without compensating for the signal loss due to bubble formation, then one would have to accommodate an important fission gas release from the grain bulk in a structure where intergranular bubbles are still closed and represent only a small fraction of the total bubble volume fraction. The uncorrected 15 kV EPMA data indicate a fractional Xe release of more than 50% at this position and the 30 kV analysis about 20%, but after correction for the geometry effects, it is seen that bulk release does not yet occur. Interconnection of grain boundary bubbles on the other hand is obvious at position $r/r_0 = 0.55$ (Fig. 16(b)). At this position, the Xe profiles also evidence the release of Xe from the grain interior.

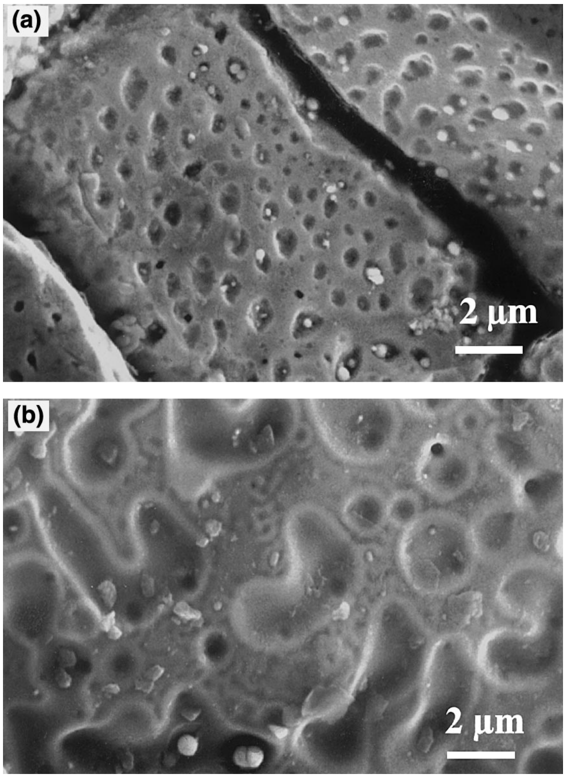

Fig. 16. Grain boundary aspect at different radial positions. (a) at radial position $r/r_0 = 0.65$: the grain boundary bubbles are closed. (b) at radial position $r/r_0 = 0.55$: grain boundary bubbles are interconnected and may vent to the intergranular pores.

The determination of the point at which gas is released from the bulk of the grains is important to interpret correctly the role that grain boundaries play in the fission gas release of this particular sample. Let us consider the following two cases in more detail. If the bulk release does not occur at the considered position $r/r_0 = 0.65$, then the gas present in grain boundary bubbles is accumulated from the adjacent areas only. The intragranular gas bubbles on the other hand accomodate the average generated amount of Xe. The other case assumes that bulk Xe release did occur to an amount of 20% at this position, which is the figure derived from the uncorrected 30 kV profile. In this case, the grain boundary bubbles have to accomodate an additional 20% of the total generated amount, while the intragranular bubbles accomodate the remaining 80%. The following geometrical parameters apply.

The intragranular bubble volume fraction (V_V) at the considered position ($r/r_0 = 0.65$) is read from Fig. 12:

$$V_V = 2.7\%. \tag{15}$$

The volume associated with a lenticular bubble of radius of curvature r_c and contact angle θ, read as

$$V_b = \frac{4\pi}{3} r_c^3 \left(1 - \frac{3}{2}\cos\theta + \frac{1}{2}\cos^3\theta\right). \tag{16}$$

The number of bubbles per unit grain boundary surface area for a given surface coverage fraction (F_S) is expressed by

$$n_b = \frac{F_S}{\pi r_c^2 \sin^2\theta}. \tag{17}$$

The internal grain boundary surface per unit of volume (S_V) is equal to

$$S_V = \frac{2}{\overline{L}_3}. \tag{18}$$

The volume fraction of grain boundary bubbles per unit of sample volume (V_{GBB}) is then finally given by

$$V_{GBB} = n_b V_b S_V. \tag{19}$$

At relative radius $r/r_0 = 0.65$, the grain boundary bubbles have the following dimensions:

$$\text{Surface coverage: } F_S = 50\%, \tag{20a}$$

$$\text{bubble diameter: } 2r_c \sin(\theta) = 600 \text{ nm}, \tag{20b}$$

$$\text{bubble width: } 2h = 2r_c(1 - \cos\theta) = 300 \text{ nm}. \tag{20c}$$

This yields the following bubble parameters: $r_c = 375$ nm and contact angle $\theta = 53°$. On the basis of the numerical values of (20a)–(20c), the volume fraction of grain boundary bubbles (V_{GBB}) at $r/r_0 = 0.65$ is calculated

$$V_{GBB} = 0.4\%. \tag{21}$$

This relatively low value is due to the fact that the large grain size of the present sample results in a small internal surface: $S_V = 5.0 \times 10^4$ m^2/m^3.

Since the diffusion coefficients for doped UO_2 are not well-known, the width of the zones that release their gas to the grain boundaries is estimated geometrically. It is assumed that a lower limit is given by the average intragranular bubble radius. All gas generated within this distance from a grain boundary is thus assumed to be accumulated in grain boundary bubbles. The amount of Xe present within a distance Δ ($\Delta = 0.150$ μm at $r/r_0 = 0.65$) from the grain boundaries is given by

$$2\Delta S_V N_{Xe}. \tag{22}$$

The atomic density of produced Xe atoms (N_{Xe}) amounts to

$$N_{Xe} = 3.52 \times 10^{26} \text{ atoms/m}^3. \tag{23}$$

With these data, one can now calculate the intragranular and grain boundary bubble pressures for the two considered cases. Using the equation of state as proposed by Brearley and MacInnes [24] for inert gases at high pressures, the following results are obtained.

If one assumes that at the considered position true bulk release did not yet occur, then the intragranular bubble pressure is calculated to be 500 MPa. In this scenario, the grain boundary bubbles accumulate the gas atoms generated close to the grain boundaries only, and their pressure is 25 MPa, which is approximately five times the equilibrium pressure for bubbles with a radius of curvature equal to 375 nm. If on the other hand, the scenario involving a 20% release from the grain interior is calculated, then the intragranular bubble pressure decreases slightly to 340 MPa, and the grain boundary bubble pressure rises to 1.04 GPa. The above calculations are only a very rough estimate of the order of magnitude for the different pressures since only geometrical effects are considered, the Kr component is neglected and bubble distributions are based on SEM observations only, while it is known that small bubbles are likely to develop but remain unresolved.

What can be learned, however, is that the scenario involving important release of fission gas from the bulk of the grains without interconnection of the grain boundary bubbles leads to a paradoxical result in which the grain boundary bubbles develop pressures that are three times higher than the intragranular bubbles. In the other scenario, the estimated pressures for intra and intergranular bubbles show a more realistic behaviour: as long as the release of fission gas from grain interior does not occur (radial position $r/r_0 = 0.65$), the grain boundary bubbles only accumulate gas from the adjacent zones, which is sufficient to build up a moderate overpressure. When gas release from the grain bulk is evident also after compensating for the loss of signal due to bubble development (radial position $r/r_0 = 0.55$), the grain boundaries interconnect (Fig. 16(b)).

4. Conclusions

Electron probe microanalysis probes the surface rather than the bulk concentration. In the specific case of gas bubbles in a solid, a concentration gradient exists close to the surface of the sample. If its influence on the apparent gas concentration is neglected, then the retained gas concentration may be underestimated. In order to account for this, we have calculated the geometry related effects on the X-ray signal. The parameters of the model are either directly determined by SEM observations, or adjusted through a full exploitation of multiple voltage analyses. The present analysis method allows one to better estimate the true retained xenon profile. Even when a full correction procedure is not imperative, one might appreciate a straightforward method that allows one to estimate to what extent the geometry influences the measured Xe signal. This can easily be achieved by applying the multiple voltage analyses proposed in this paper. The difference in measured signal when a different accelerating voltage is applied provides a rapid method to evaluate in a qualitative way to what extent the microstructure influences the measurements.

In the examples presented in this study, the multiple voltage analyses have shown that the EPMA profile is not influenced by the applied accelerating voltage when intragranular bubbles do not develop or is only marginally affected when intragranular bubbles rapidly vent to the grain boundaries. On the other hand, in cases where a considerable fraction of the fission gas is retained in intragranular bubbles, as in the case with transient tested, large grained fuel, the measured Xe signal may be highly influenced by the intragranular bubble evolution. After correcting the Xe concentration profiles of the latter sample for geometrical influences on the X-ray intensity, it is seen that true fission gas release occurs at higher temperatures (i.e., more towards the pellet centre) than estimated from raw data. The calculated retained gas fraction raises accordingly. At low accelerating voltages, the retained gas fraction is highly underestimated, but the signal loss due to geometrical factors decreases if higher accelerating voltages are applied. One may thus assume that the application of an elaborate correction procedure is not always justified if only a gross profile is searched after. This was also remarked by Walker and co-workers [2,5], who decided no longer to apply the correction procedure developed by Ronchi and Walker [3] and rather to rely upon profiles acquired at elevated accelerating voltages.

On the other hand, the full correction procedure has proven to be indispensable in the confrontation of the Xe profile with observations of the grain boundary bubble evolution. A direct interpretation of the uncorrected data, even those acquired at an accelerating voltage of 30 kV, would have led to the conclusion Xe is released from the grain interior at positions where interlinkage of bubbles was still absent. After correction for the influence of bubble formation on the X-ray signal, the Xe profile shows that release of Xe from the grain interior occurs with the simultaneous interlinkage of grain boundary bubbles.

Acknowledgements

Fruitful discussions with M. Lippens, C.T. Walker, P. Van Uffelen and A. Delbrassine are gratefully acknowledged. The author is also indebted to F. Swinnen and B. Vos for sample preparation and analyses.

References

[1] Hj. Matzke, H. Blank, M. Coquerelle, K. Lassmann, I.L.F. Ray, C. Ronchi, C.T. Walker, J. Nucl. Mater. 166 (1989) 165.
[2] C.T. Walker, P. Knappik, M. Mogensen, J. Nucl. Mater. 160 (1988) 10.
[3] C. Ronchi, C.T. Walker, J. Phys. D 13 (1980) 2175.
[4] M. Mogensen, C.T. Walker, I.L.F. Ray, M. Cocquerelle, J. Nucl. Mater. 131 (1985) 162.
[5] C.T. Walker, J. Nucl. Mater. 275 (1999) 56.
[6] J.L. Pouchou, F. Pichoir, K.F.J. Heinrich, D.E. Newbury, Electron Probe Quantitation, Plenum, New York, 1991, p. 31.
[7] C.T. Walker, J. Nucl. Mater. 80 (1979) 190.
[8] S.J.B. Reed, Electron Microprobe Analysis, Cambridge University, Cambridge, 1993.
[9] J. Philibert, J. Métaux, 465 (1964) 157.
[10] R.H. Packwood, J.D. BrownD.B. Wittry, Microbeam analysis – 1980, San Fransisco Press, San Fransisco, 1980.
[11] S. Tanuma, K. Nagashima, Mikrochim. Acta 1 (1983) 299.
[12] G. Love, D.A. Sewell, V.D. Scott, J. Phys. (Paris) 45 (C2) (1984) 21.
[13] J.L. Pouchou, F. Pichoir, J. Phys. (Paris) 45 (C2) (1984) 17.
[14] J.L. Pouchou, F. Pichoir, J. Phys. (Paris) 45 (C2) (1984) 47.
[15] G.F. Bastin, H.J.M. Heijliggers, F.J.J. Van Loo, Scanning 8 (1986) 45.
[16] E.E. Underwood, Quantitative Stereology, Addison-Wesley, MA, 1976.
[17] K.J.F. Heinrich, in: Proceedings of the 11th International Conference on X-ray Optics and Microanalysis, University of Western Ontario, 1986, p. 67.
[18] L.E. Thomas, S.E. Donnelly, J.H. Evans, Fundamental Aspects of Inert Gases in Solids, Plenum, New York, 1991, p. 431.
[19] S. Kashibe, K. Une, K. Nogita, J. Nucl. Mater. 206 (1993) 22.
[20] D.R. Olander, Fundamental aspects of nuclear reactor fuel elements, Technical Information Centre, Office of Public Affairs, Energy Research and Development Administration, 1976, p. 339.

[21] I.L.F. Ray, H. Thiele, Hj. Matzke, J. Nucl. Mater. 188 (1992) 90.

[22] J.H. Evans, A. Van Veen, K.T. Westerduin, J. Nucl. Mater. 195 (1992) 250.

[23] M. Mogensen, J. Als-Nielsen, N.H. Anderson, Determination of fission products in irradiated fuel by X-ray fluorescence, report Riso-M-2599, 1986.

[24] I.R. Brearly, D.A. MacInnes, J. Nucl. Mater. 95 (1980) 239.